Bioactive Materials 52 (2025) 829–844

Contents lists available at ScienceDirect

Bioactive Materials

journal homepage: www.keaipublishing.com/en/journals/bioactive-materials

Amorphous calcium zinc phosphate promotes macrophage-driven alveolar bone regeneration via modulation of energy metabolism and mitochondrial homeostasis

Shuze Wang [a,b,1], Lei Cao [c,d,1], Caihao Huang [c,d], Junyi Wang [a,b], Jialin Liu [a,b], Yeyuan Wang [a,b], Qiang Wang [a,b,*], Qing Zhou [a,b], Xing Zhang [c,d,**], Dan Zhang [a,b,***]

[a] School and Hospital of Stomatology, China Medical University, Shenyang, Liaoning, 110001, China
[b] Liaoning Provincial Key Laboratory of Oral Diseases, China Medical University, Shenyang, Liaoning, 110001, China
[c] Institute of Metal Research, Chinese Academy of Sciences, Shenyang, Liaoning, 110016, China
[d] School of Materials Science and Engineering, University of Science and Technology of China, Shenyang, Liaoning, 110016, China

ARTICLE INFO

Keywords:
Alveolar bone healing
Amorphous calcium zinc phosphate
Single-cell RNA sequencing
Macrophage
Mitochondria

ABSTRACT

The repair of alveolar bone defects continues to pose a significant challenge within the field of stomatology. As the primary implant material utilized in clinical treatment, the mechanisms by which calcium phosphate-based materials promote bone formation necessitate further in-depth exploration. Single-cell RNA sequencing was employed to characterize the immune microenvironment surrounding hydroxyapatite (HA)-mediated alveolar bone regeneration, confirming the macrophage-dependent enhancement of regenerative outcomes. Based on this finding, amorphous calcium zinc phosphate (ACZP) nanoparticles were developed as immunomodulatory nanomaterials. ACZP can accelerate bone regeneration via anti-inflammatory phenotype polarization, specifically by inhibiting endoplasmic reticulum-mitochondria coupling, reducing pathological Ca^{2+} transfer, and shifting macrophage metabolism from glycolysis to oxidative phosphorylation (OXPHOS), thereby enhancing bioenergetics. Our results demonstrated that ACZP can inhibit the IP3R/MCU pathway in macrophages, restoring their anti-inflammatory capabilities and ultimately achieving significant effects in the alveolar bone defects of New Zealand white rabbits. Twelve weeks post-surgery, the defects in the ACZP group were filled with nearly 70 % newly formed bone tissue. This study elucidated the immunomodulatory role of ACZP materials in the dynamic process of alveolar bone healing, providing novel insights and methodologies for the design of materials in the fields of tissue engineering and regenerative medicine.

1. Introduction

The effectiveness of alveolar bone defect repair significantly relies on optimizing the biological properties of the implanted materials [1]. The immune response to the implanted materials is crucially important for the healing of alveolar bone defect [2]. Macrophages, the most abundant immune cells in tissues, play an essential role in maintaining the homeostasis of the inflammatory environment [3]. The behavior of macrophages is highly dependent on the transition of metabolic patterns. Pro-inflammatory macrophages primarily utilize the aerobic glycolysis pathway for rapid energy supply, whereas anti-inflammatory macrophages depend more on oxidative phosphorylation (OXPHOS) to ensure sufficient energy availability [4]. This highlights the crucial role of mitochondrial function in the transformation of macrophage behavior [5]. Therefore, the development of biomaterials that support macrophage mitochondrial function can contribute to improved outcomes in

Peer review under the responsibility of editorial board of Bioactive Materials.
* Corresponding author. School and Hospital of Stomatology, China Medical University, Shenyang, Liaoning, 110001, China.
** Corresponding author. Institute of Metal Research, Chinese Academy of Sciences, Shenyang, Liaoning, 110016, China.
*** Corresponding author. School and Hospital of Stomatology, China Medical University, Shenyang, Liaoning, 110001, China.
E-mail addresses: mfqwang@cmu.edu.cn (Q. Wang), xingzhang@imr.ac.cn (X. Zhang), 20052054@cmu.edu.cn (D. Zhang).
[1] These authors contributed equally to this work.

https://doi.org/10.1016/j.bioactmat.2025.06.053
Received 21 May 2025; Received in revised form 23 June 2025; Accepted 25 June 2025

bone repair [6,7].

Hydroxyapatite (HA), a widely utilized active bioceramic material, exhibits osteoconductivity and demonstrates a close interaction with cells and tissues within the physiological environment [8]. However, Dorozhkin et al. discovered that HA was the most stable and least soluble or degradable among calcium orthophosphates ($-\log(K_{sp}) = 116.8$ at 25 °C) [9]. Proussaefs et al. evaluated the histology of HA specimens retrieved from human subjects after implantation for nine years, finding that the residual HA particles exhibited no signs of absorption [10]. Shanley et al. found that micron-size HA particles upregulated glycolysis markers, including the glucose transporter-1 (GLUT1), hexokinase 2 (HK2), and pyruvate kinase M2 (PKM2) [11]. This low degradability and the pro-inflammatory polarization of macrophages restrict broad clinical applications of HA. However, the molecular mechanisms underlying the dynamic interactions between HA and macrophages during tissue repair remain largely unexplored. Single-cell RNA sequencing (scRNA-seq), with its high-throughput capabilities and single-cell resolution, facilitates a comprehensive analysis of transcriptomic expression at the cellular level [12]. This approach characterizes the molecular and cellular dynamics of HA-based biomaterials in the repair of alveolar bone defects, particularly concerning cell heterogeneity, functional changes, and intercellular communication [13]. By optimizing the osteo-immunomodulatory properties of HA materials through scRNA-seq, we can significantly enhance their efficacy in repairing alveolar bone defects. Consequently, the development of macrophage-friendly biomaterials with high degradation properties will provide substantial support for high-quality alveolar bone repair. The most prevalent strategy was enhancing the solubility of the HA phase or combining with materials that possess complementary properties, thereby providing synergistic effects to develop multifunctional composites.

Amorphous calcium phosphate (ACP), recognized as a precursor of HA, exhibits a resorption rate that aligns more closely with new bone formation and demonstrates superior osteoconductivity *in vivo* compared to HA [14]. Previous studies have investigated the solubility of different calcium phosphate phases under the physiological conditions of osteoclastic bone resorption, specifically within a pH range of 4–5, revealing that the solubility of ACP significantly exceeds that of HA [15]. Moreover, ACP can be ustilized for the delivery of drug molecules due to favorable degradability [16]. In a previous study, we established a method to maintain the amorphous state of ACP particles, thereby laying a foundation for subsequent loading of cell-targeted bioactive particles [17]. The dynamic changes in mitochondria play a pivotal role in regulating intracellular calcium signaling [18]. The particle size of ACP spheres or spheroids is typically below 200 nm [19]. Consequently, ACP nanoparticles, which exhibit higher solubility, are more readily phagocytosed and possess a superior capacity for calcium ion release compared to HA, thereby eliciting a pronounced cellular metabolic response. Based on these findings, our objective is to develop a method to stabilize mitochondrial calcium balance and enhance the compatibility of biomaterials with macrophages.

As a cofactor of ATP, zinc profoundly influences mitochondrial function by regulating glycolysis and OXPHOS, playing a critical role in bone metabolism, essential for normal bone development [20]. Fu et al. found that mesenchymal stem cells (MSCs) absorb and utilize zinc ions to regulate their osteogenic differentiation, providing an important theoretical basis for employing zinc ions as an active ingredient for bone repair [21]. In addition, zinc ions not only directly promote bone formation but also regulate macrophage function and immune responses. Tan et al. demonstrated that Zn^{2+} concentrations within the range of 11.25–45 μM promoted the polarization of macrophages toward the anti-inflammatory phenotype, while inhibiting polarization toward the pro-inflammatory phenotype [22]. Meanwhile, Hershfinkel et al. discovered the connection between zinc-dependent calcium regulation and the formation of inositol trisphosphate (IP3) in cells [23]. Consequently, we propose that a zinc-rich microenvironment will enhance the osteogenic efficacy of ACP through cellular mitochondrial energy metabolism.

In this study, we utilized scRNA-seq to investigate the effects of HA on the behavior of macrophages during the alveolar bone repair process. Concurrently, amorphous calcium zinc phosphate (ACZP) nanoparticles were synthesized via a wet chemical method. The biocompatibility and immunomodulatory effects of ACZP were systematically evaluated through *in vitro* experiments with RAW264.7 macrophage cells. By integrating metabolomics, we explored the regulatory effects of ACZP on macrophage metabolism and mitochondrial homeostasis, and the underlying mechanisms influencing the IP3R/MCU calcium ion channel pathway. Additionally, *in vivo* animal experiments were conducted using a rabbit alveolar bone defect model, complemented by micro-CT imaging and histological analysis, to validate the efficacy of ACZP in repairing bone defects. This study emphasizes the critical role of metabolically active ions in cell-material interactions and underscores the importance of mitochondrial behavior and homeostasis in alveolar bone healing.

2. Results

2.1. The effects of HA nanoparticles on macrophage anti/pro-inflammatory phenotype transformation

The classic rod-like HA nanoparticles were synthesized using the wet chemical method to evaluate the dynamic effects on bone formation in alveolar bone defect areas comprehensively [24,25]. The average particle size of the HA samples was 72.4 ± 0.6 nm (Fig. 1A and Fig. S1A), and the zeta potential of −21.3 mV indicated good dispersibility. The X-ray diffraction (XRD) pattern (Fig. S1B) confirmed that the samples were composed of HA crystals (JCPDF #09–0432). To comprehensively evaluate the dynamic effects of different calcium phosphate-based materials on bone formation in alveolar bone defect areas, scRNA-seq was applied to analyze cells from the defect regions in mice on day 7 from the HA group (filled with HA), or from the Control group (no treatment) (Fig. 1A). Cells were classified into 12 clusters based on cell surface markers, including natural killer T cells (T_NK cells) (*Cd3d*), B cells (*Cd19*), dendritic cells (DCs) (*Cd209a*), monocyte_macrophages (Mono_Mac) (*Cd68*), granulocyte-monocyte progenitors (GMP) (*Mpo*), neutrophils (*G0s2*), mesenchymal stem cells (MSCs) (*Cxcl12*), fibroblasts (*Dcn*), osteoclasts (*Mmp9*), osteoblasts (*Bglap*), erythrocytes (*Gypa*), and mast cells (*Mcpt8*) (Fig. 1B).

Visualization using t-distributed stochastic neighbor embedding (t-SNE) revealed that neutrophils and monocyte-macrophages constituted the primary cell populations within the defect area. Notably, the proportion of macrophages in the HA group (13.30 %) was significantly higher than that in the Control group (9.83 %) (Fig. 1C). To investigate the immunomodulatory effects of calcium phosphate on macrophages in the bone defect area, we classified *Cd68*^{high} cells into four functional subsets (M1–4) based on their differential gene expression profiles and characteristic markers: Macrophage 1 (*C1qc, Mrc1*), Macrophage 2 (*Plac8, Vcan*), Macrophage 3 (*Elane, Prtn3*) and Macrophage 4 (*Marco, Cd163*) (Fig. 1B–S2A, B).

The gene expression profile indicated that Macrophage 1 exhibited elevated levels of gene expression for markers such as *Cd206* and Arg*1,* reflecting significant anti-inflammatory characteristics. In contrast, Macrophage 2 was characterized by elevated expression of inflammatory response-related genes, including *Ifitm6,* etc. Macrophage 3 showed upregulation of genes such as *Ctsg* and *Mpo,* etc., which exacerbated tissue damage by promoting the release of proteases and pro-inflammatory factors. Conversely, Macrophage 4, with high expression of *Marco* and *Cd163,* etc., exhibited anti-inflammatory and reparative functions, alleviating inflammation by inhibiting neutrophil adhesion and activation (Fig. S3). Furthermore, the proportion of anti-inflammatory macrophages (Macrophage 1 and 4) in the alveolar bone defects was reduced in the HA group (68.35 %) compared to the Control

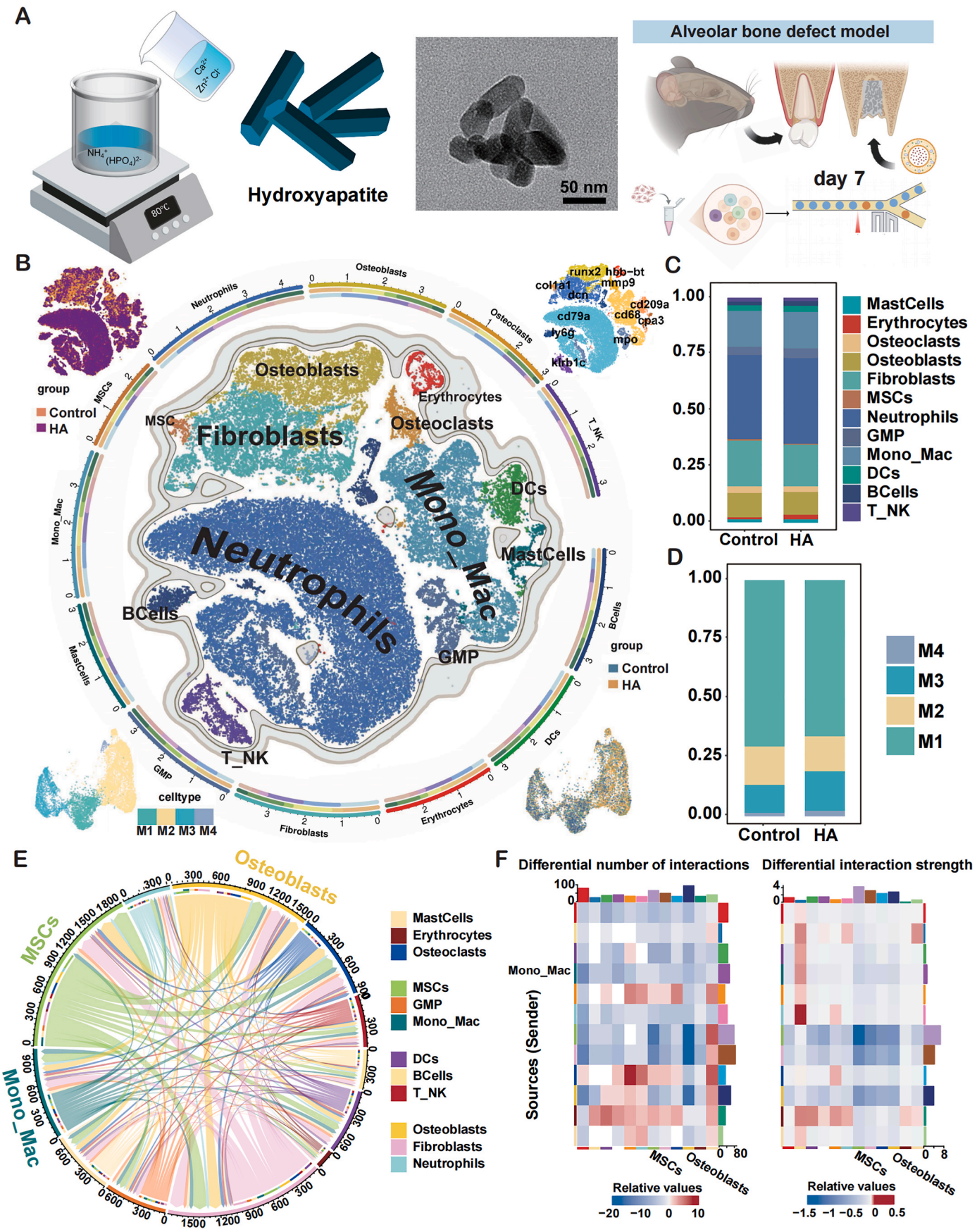

(caption on next page)

Fig. 1. Synthesis of HA nanoparticles and verification of their induction effect on the polarization of pro-inflammatory macrophages in the alveolar bone defect area through scRNA-seq: (A) Schematic diagram of the procedure for preparing scRNA-seq samples of HA implants in mouse mandibular alveolar bone defects; (B) t-SNE plot (centre) showed cells from six pooled samples, colored by cell type. Inset images in the four corners, clockwise from the upper left, display the sample source, t-SNE plots of marker gene expression, and characteristic UMAP atlas of different samples and cell subpopulations of macrophages. (C) Proportions of different cell types in each group. (D) Proportion of each macrophage cluster in different groups. (E) Network diagram of cell communication. The thickness of the line represented the interaction number of cells between the line. (F) Differences in intercellular communication between the Control and HA groups. Heatmaps of the number and strength of receptor-ligand pair signals among different cells. Red, up-regulated in the Control group. Blue, down-regulated in the Control group.

group (74.10 %). This finding suggested that HA implantation resulted in inadequate conversion of anti-inflammatory macrophages in the defect area, potentially contributing to chronic inflammation and tissue damage (Fig. 1D). To investigate the mechanisms by which macrophages influenced bone defect repair, we analyzed cell-cell communication, focusing on the interactions between different cell types following HA implantation in the defect. Significant interactions were observed between macrophage populations, and MSCs and osteoblasts (Fig. 1E). Compared to the Control group, both the number and intensity of signaling pathways were markedly enhanced in the HA group (Fig. 1F–S4). At both 7 and 14 days following HA implantation, the expression of the pro-inflammatory marker iNOS was significantly elevated, while the fluorescence intensity of the anti-inflammatory marker Arg1 was comparatively weak. Meanwhile, inflammatory fibers were observed at the center of the bone defect (Fig. S5). These results indicate that the implantation of HA can disrupt the transformation of macrophages between anti/pro-inflammatory phenotype transformation of macrophages in the bone defect area due to its low degradability, resulting in poor repair of bone defects.

2.2. The glycolytic metabolic reprogramming and mitochondrial dysfunction triggered by HA

Macrophages consume a substantial amount of energy when performing phagocytosis and secretion functions, and their polarization process is highly dependent on metabolism. Gene Ontology (GO) enrichment analysis revealed significant differences in the enrichment of macrophages between the Control and HA groups in pathways related to “metabolic process” and “membrane-bounded organelle” (Fig. 2A). Gene scores were employed to quantify glycolytic and OXPHOS pathway activities in macrophages. A significant elevation in glycolytic scores was observed in all macrophage clusters following HA implantation (Fig. 2C and D). In contrast, the OXPHOS scores were suppressed in the HA group (Fig. 2B). Furthermore, elevated expression levels of glycolytic pathway-associated genes were observed in the HA group compared to the Control group, especially the expression of *Pkm*, a key regulatory factor in the glycolysis pathway, which increased significantly (Fig. 2E and F). These results further confirmed that macrophage metabolic reprogramming was substantially modulated by HA implantation. Mechanistically, HA induced the conversion of macrophages to the pro-inflammatory phenotype by activating the glycolysis pathway rather than the OXPHOS pathway.

Pseudotime analysis was subsequently conducted to further investigate the influence of bone healing progression on macrophage differentiation. A pseudotemporal trajectory was reconstructed based on the kinetics of macrophage gene expressio, revealing two distinct branching points that defined four transcriptionally heterogeneous clusters. These clusters were mapped along the developmental continuum, with Macrophage 3 demonstrating the earliest pseudotime positioning, suggesting its potential role as the progenitor state for subsequent subcluster differentiation. Macrophage 1 and 2 exhibited separate branches, with Macrophage 1 being more widely distributed and partially overlapping with Macrophage 4 (Fig. 2H–S6). Consequently, pro-inflammatory macrophages identified at the trajectory terminus were classified as belonging to the Fate 1 branch, while anti-inflammatory macrophage populations were localized to the opposing terminus, constituting the Fate 2 branch. Gene expression kinetics analysis revealed that within the Fate 1 branch, genes activated during the terminal phase of cellular transition were predominantly associated with GO terms linked to oxidative stress and mitochondrial homeostasis, including “mitophagy”, “HIF-1 signaling pathway” and “NOD-like receptor signaling pathway”, etc (Fig. 2G). GO analysis further validated the distinct mitochondrial functional profiles between the HA group and the Control group. Significant enrichment was observed in biological processes associated with “mitochondrial membrane homeostasis”, “oxidative respiratory chain impairment”, and “mitochondrial reactive oxygen species (mtROS) generation” (Fig. 2I). These findings indicated that the phenotypic transformation of alveolar bone macrophages was notably correlated with mitochondrial-related gene expression patterns. Specifically, the transformation to a pro-inflammatory phenotype, induced by OXPHOS interruption, was hypothesized to be driven by mitochondrial homeostasis disruption and exacerbated mitochondrial dysfunction.

2.3. Synthesis and characterization of ACZP nanoparticles as an immunomodulatory nanoplatform for bone regeneration

The ACZP nanoparticles, assembled with the mediation of polyacrylic acid (PAA) molecules, were utilized to modulate macrophage phenotypes within the defect area. These ACZP nanoparticles were synthesized using a wet chemical method by doping zinc ions at various molar ratios, resulting in the formation of 5Zn-ACP, 10Zn-ACP, and 20Zn-ACP, which exhibited good stability through the chelation of PAA at room temperature (Fig. 3A).

Transmission electron microscope (TEM) bright field images at high magnification revealed the 5Zn-ACP, 10Zn-ACP, 20Zn -ACP nanoparticles ranged from 15.0 to 33.1 nm (Fig. 3B–S7). The electron diffraction pattern of the selected area confirmed the amorphous state of the 5Zn-ACP nanoparticles. The XRD patterns of 5Zn-ACP,10Zn-ACP, and 20Zn-ACP further indicated the amorphous state of these nanoparticles (Fig. 3C). The Fourier transform infrared (FTIR) results showed characteristic peaks of the stretching vibration of carboxyl group in PAA molecules at 1556 $cm^{-1}$and 1455 cm^{-1}. The bands of P-O stretching vibration from the PO_4^{3-}group located at1001 cm^{-1}, whereas the bands of the P-O bending vibration located at 548 cm^{-1} (Fig. 3D). X-ray photoelectron spectroscopy (XPS) was used to further illustrate the chemical state and elemental composition of ACZP samples, which showed the presence of Zn, Ca, O and P elements (Fig. 3E–S8). Meanwhile, the contents of zinc in the 5Zn-ACP, 10Zn-ACP, 20-ACP samples were also tested by inductively coupled plasma mass spectrometry (ICP-MS), as shown in Table S1. In order to analyze the content of bound water, TG/DSC analysis of ACZP samples was conducted from room temperature to 700 °C. The inside bound water of 5Zn-ACP, 10Zn-ACP, 20Zn-ACP samples approximately 15.1 wt%, 16.3 wt% and 17.2 wt% were lost between 30 °C and 315 °C. The combustion reaction of PAA molecules occurred between 315 °C and 400 °C corresponding to the DSC curves with the weight loss of 9.2 wt%, 9.7 wt% and 10.7 wt% for 5Zn-ACP, 10Zn-ACP, 20Zn-ACP samples, respectively (Fig. 3F and G). ACP was more unstable than calcium phosphate crystals such as β-tricalcium phosphate (β-TCP) and HA [9]. In this study, 5Zn-ACP nanoparticles were dissolved in PBS for 30 days, thereby mimicking their release during implanting (Fig. S9). When the 5Zn-ACP sample was dissolved for 1 day, the released concentrations of Ca^{2+} and Zn^{2+} ions were 21.3 μg/mL and 2.5 μg/mL. With the extension of time, the release concentrations of calcium ions and zinc ions were 37.6 μg/mL and 5.2 μg/mL on the seventh day. The majority of calcium and zinc ions could

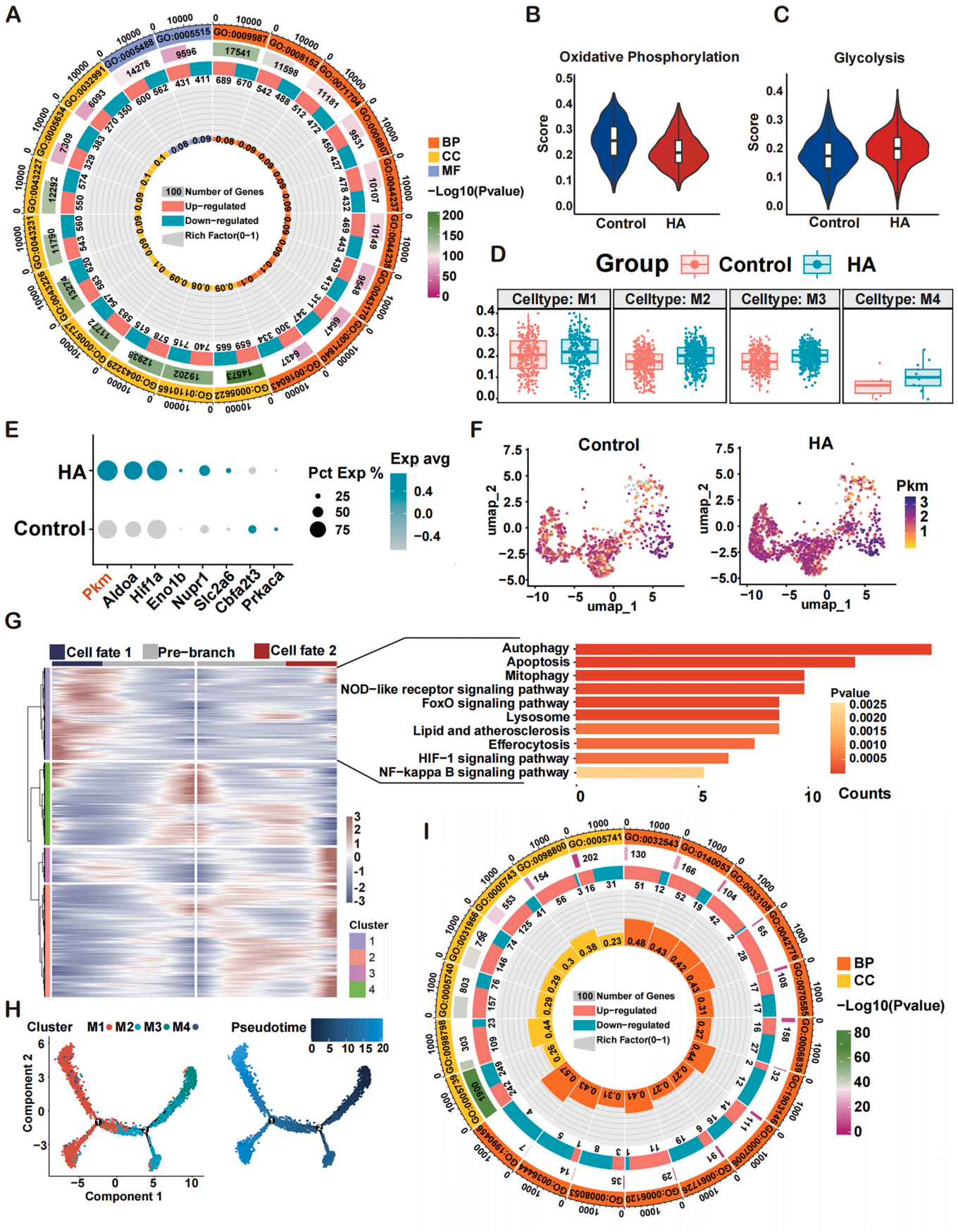

(caption on next page)

Fig. 2. The dynamic changes in macrophage metabolism and mitochondrial function induced by HA: (A) GO analysis showed the top 20 biological function differences of macrophages between the HA and Control groups. In the outermost classification track, colors represent different classifications: red indicated biological process (BP), yellow indicated cellular component (CC), and blue indicated molecular function (MF). The scale represented the total number of genes. The length of the rectangle indicates the number of genes included in that term. The innermost rectangle represented the enrichment *P*-value of that term (Values were presented as $-\log_{10}$(*P*-value)). (B) Violin plots showed the characteristic scores of OXPHOS in macrophages between the HA and Control groups. (C) Violin plots showed the characteristic scores of glycolysis in macrophages between the HA and Control groups. (D) GO scores of the OXPHOS pathway among all macrophage subpopulations between the HA and Control groups. (E) Glycolysis genes expressed by macrophages in alveolar bone defects between the HA and Control groups. The size of the dots represents the proportion of cells expressing each gene, and the color of the dots reflects the expression level. (F) UMAP atlas and showed the expression of the *Pkm* gene in the HA and Control groups. (G) Heatmap showed the scaled expression of differently expressed genes between the HA and Control groups in three branches as in (H), cataloged into four major gene clusters (labels on right) that varied as a function of pseudotime, highlighting unique response pathways in gene cluster1 along the right margin. (H) Trajectory order of the macrophage populations by pseudotime value. (I) GO analysis showed the top 20 mitochondrial-related function differences of macrophages between the HA and Control groups.

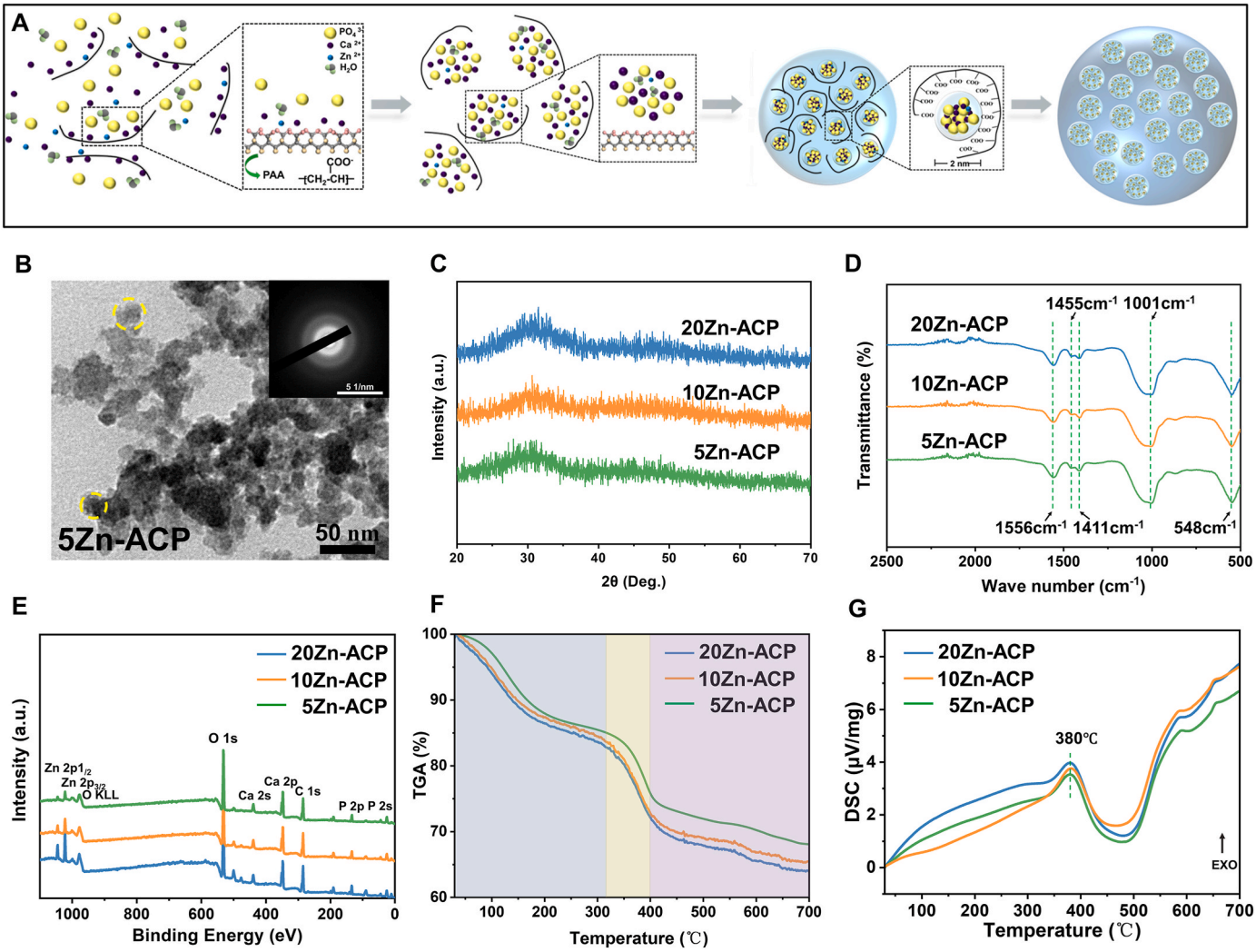

Fig. 3. Characteristics of synthesized ACZP nanoparticles: (A) Schematic diagram of the progressive assembly of ACZP nanoparticles. (B) Bright field image of 5Zn-ACP by TEM. The sizes of the specific grains were marked with yellow dashed circles. (scale bar: 50 nm). (C) XRD patterns of Zn-ACP. (D) FTIR of Zn-ACP. (E) XPS spectra of Zn-ACP. (F) Thermogravimetric analysis (TGA) of ACZP. (G) Differential scanning calorimetry (DSC) of ACZP.

be released within 30 days.

The *in vitro* interactions between ACZP and macrophages were evaluated. Fluorescence microscopy revealed significant cell death in the 20Zn-ACP group after 24 h, while the other groups exhibited nearly 100 % cell survival (Fig. S10A). Cell counting kit-8 (CCK-8) assays demonstrated that macrophage proliferation increased in the HA, 5Zn-ACP, and 10Zn-ACP groups over the course of 1, 2, and 3 days of co-culture (Fig. S10B). These findings suggest that ACZP effectively promotes cell proliferation with appropriate zinc content. In addition, the effects of varying concentrations of ACZP on macrophage polarization were investigated *in vitro*. Immunofluorescence analysis revealed that in the HA group, a higher proportion of cells expressed the pro-inflammatory polarization marker iNOS, while the expression of the anti-inflammatory marker Arg1 was relatively low. However, the incorporation of Zn^{2+}, especially in the 5Zn-ACP group, significantly mitigated this pro-inflammatory polarization, leading to a notable increase in Arg1 expression (Fig. S10C and D). To investigate the impact of the immune microenvironment established by different nanoparticles on osteogenesis, the 7-day and 14-day Alkaline phosphatase (ALP) staining experiment was conducted, demonstrating a higher density of calcium

deposition in the 5Zn-ACP group (Fig. S10E). In summary, 5Zn-ACP achieved an optimal balance between biocompatibility and immune microenvironment regulation, which was mainly used for further study.

2.4. ACZP alleviates calcium phosphate-induced energy metabolism dysregulation through restoration of mitochondrial respiratory chain activity

The key metabolites of macrophages exposed to HA/ACZP powder extracts and complete culture medium were utilized for further investigation to reveal whether the addition of Zn^{2+} ions could enhance the polarization of HA-treated macrophages through metabolic regulatory pathways. The volcano plot of the two groups showed the characteristic differences related to HA (Fig. 4A). Heatmap analysis and Kyoto Encyclopedia of Genes and Genomes (KEGG) enrichment analysis results indicated that compared with macrophages treated with diluted ACZP solution, the contents of some important markers of pro-inflammatory macrophages and key glycolytic metabolites such as citrate, lactate, malate, and glucose-6-phosphate increased in cells exposed to HA (Fig. 4B and C). The changes in key cellular metabolites and their positions within the glycolysis and tricarboxylic acid cycles were shown in Fig. 4D, illustrating the accumulation and consumption of these metabolites.

To explore this mechanism in depth, we monitored the oxygen consumption rate (OCR) and extracellular acidification rate (ECAR) of RAW264.7 cells to evaluate the metabolic characteristics of macrophages under HA and ACZP conditions (Fig. 4E and F). Compared to the Control group and the ACZP group, the basal respiration ($P < 0.01$, $P < 0.05$), maximal respiration ($P < 0.001$, $P < 0.01$), and ATP production ($P < 0.01$) of the HA group were significantly lower (Fig. S11A). At the same time, the glycolytic capacity ($P < 0.01$) and glycolytic reserve capacity ($P < 0.001$, $P < 0.01$) in the HA group were significantly enhanced, compared with those in the Control group and the ACZP group (Fig. S11B). These findings revealed that macrophages treated with HA were more dependent on glycolysis, while ACZP could induce rapid metabolic reprogramming in macrophages, characterized by a continuous transition between glycolysis and OXPHOS.

To further investigate the relationship between HA-induced pro-inflammatory macrophage polarization and mitochondria, as well as the role of Zn^{2+} ions in this process, the depolarization of mitochondrial membrane potential (MMP), the initiation of mitophagy, and the activation of inflammasomes were regarded as the primary evaluation indicators. Utilizing the JC-1 probe, the addition of Zn^{2+} ions reversed the significantly enhanced green fluorescence signal compared to the HA group, resulting in a substantial increase in green fluorescence (Fig. 4H). Furthermore, mitochondria exhibited more fragmentation and elongated morphology in macrophages treated with HA. In contrast, macrophages treated with ACZP displayed punctate and short rod-shaped mitochondria, indicating that Zn^{2+} ions help alleviate the formation of elongated mitochondrial structures, thereby protecting the integrity and morphology of the mitochondrial network (Fig. 4G). Meanwhile, compared to the ACZP group, the colocalization of mitochondria and lysosomes in the HA group was significantly reduced, leading to a decreased efficiency of dysfunctional mitochondrial clearance (Fig. 4I). TEM further showed that macrophages showed mitochondrial swelling in the HA group, which were unable to effectively remove these functionally impaired mitochondria, whereas ACZP treatment restored autophagy in damaged mitochondria, thereby enhancing mitochondrial quality control and maintaining mitochondrial homeostasis (Fig. S11C).

Furthermore, we observed the immunofluorescent labeling of the NOD-like receptor thermal protein domain associated protein 3 (NLRP3) inflammasome and activated protease Caspase-1 (Fig. 4J–S11D). The ACZP group significantly inhibited the production of the inflammasome and effectively suppressed the expression of NLRP3 and Caspase-1. Since the activation of the inflammasome in macrophages is closely associated with the release of mitochondrial reactive oxygen species (mtROS), we utilized the fluorescent probe Mito-SOX to measure mtROS levels. The results indicated that HA implantation resulted in a significant accumulation of mtROS in macrophages. Notably, the peak fluorescence intensity in the ACZP group shifted to the left and surpassed that of the Control group, suggesting that Zn^{2+} exhibited a potent mtROS scavenging effect, thereby significantly alleviating oxidative stress in macrophages (Fig. S11E). In summary, Zn^{2+} ions play a crucial role in alleviating issues caused by HA, including excessive mtROS production, inflammatory responses, mitochondrial dysfunction, as well as associated complications.

2.5. ACZP disrupts IP3R/MCU-mediated ER-mitochondria calcium crosstalk to attenuate mitochondrial dysfunction and pro-inflammatory polarization

Our previous finding confirmed that HA disrupted the function of the mitochondrial respiratory chain. Changes in calcium ion transport functions in macrophages are crucially important for potential molecular mechanisms. The results of GO enrichment analysis indicated significant enrichment in terms such as “mitochondrial calcium ion homeostasis” and “intramitochondrial calcium ion transport” (Fig. 5A). Notably, there were also significant differences in the pathways encoding Ca^{2+} signal transduction and homeostasis maintenance related to IP3R, which corresponds to the function of the MCU on the endoplasmic reticulum (ER). The genes encoding the MCU complex, such as *Micu1, Vdac1*, and *Mcur1*, were significantly upregulated in the HA group (Fig. 5B). Similarly, *Itpr2* also showed a trend of differential expression. These findings suggest that HA may promote a close connection between the ER and mitochondria in macrophages by enhancing the expression of the IP3R/MCU complex, which regulated Ca^{2+} signal transduction and led to abnormal calcium ion transport, thereby affecting mitochondrial function and ultimately causing macrophage transformation into the pro-inflammatory phenotype. UMAP atlas and violin plots further verified this result: the expression levels of *Micu1* were significantly higher in the HA group than in the Control group (Fig. 5C and D). Therefore, it is crucially important to investigate whether ACZP can reshape macrophage metabolism by regulating Ca^{2+} transport between the ER and mitochondria, thereby modulating their polarization phenotype.

To predict the binding ability of inositol 1,4,5-triphosphate receptor (IP3R) and mitochondrial calcium uniporter (MCU) in different groups, molecular docking simulations were conducted to visualize the two-dimensional results (Fig. 5E). In the HA group, the binding affinity between IP3R and MCU was the highest (−32.0 kJ/mol). However, this binding affinity decreased in the ACZP group, falling below that of the Control group. By labeling and analyzing with the Mito-Tracker and ER-Tracker, the co-localization of the ER and mitochondria increased in macrophages cultured with HA, indicating a greater presence of ER-mitochondria contact sites (Fig. 5E). The addition of Zn^{2+} significantly reduced HA-induced mitochondrial elongation, enhanced the adhesion between the ER and mitochondrial membranes, and effectively reduced the presence of mitochondrial-associated membranes (MAMs). This reduction in this structure indirectly indicated a decrease in the binding affinity between these two proteins. To further evaluate the interaction between IP3R and MCU, we conducted a co-immunoprecipitation (CO-IP) analysis (Fig. S12A). The protein binding levels in the immunoprecipitated samples from the ACZP group, using the corresponding isotype control antibody, were lower compared to those in the HA group. This finding suggests that the addition of ACZP may attenuate the interaction between MCU and IP3R in macrophages.

To further validate the effect of IP3R on macrophage polarization and differentiation, Western blot analysis and immunofluorescence stainings revealed that the expression of iNOS significantly increased in the IP3R agonist group after 3 days of ACZP co-culture. In contrast, the expression of iNOS decreased following co-culture with IP3R inhibitors in the HA group (Fig. S12B–D). Furthermore, the fluorescence intensity

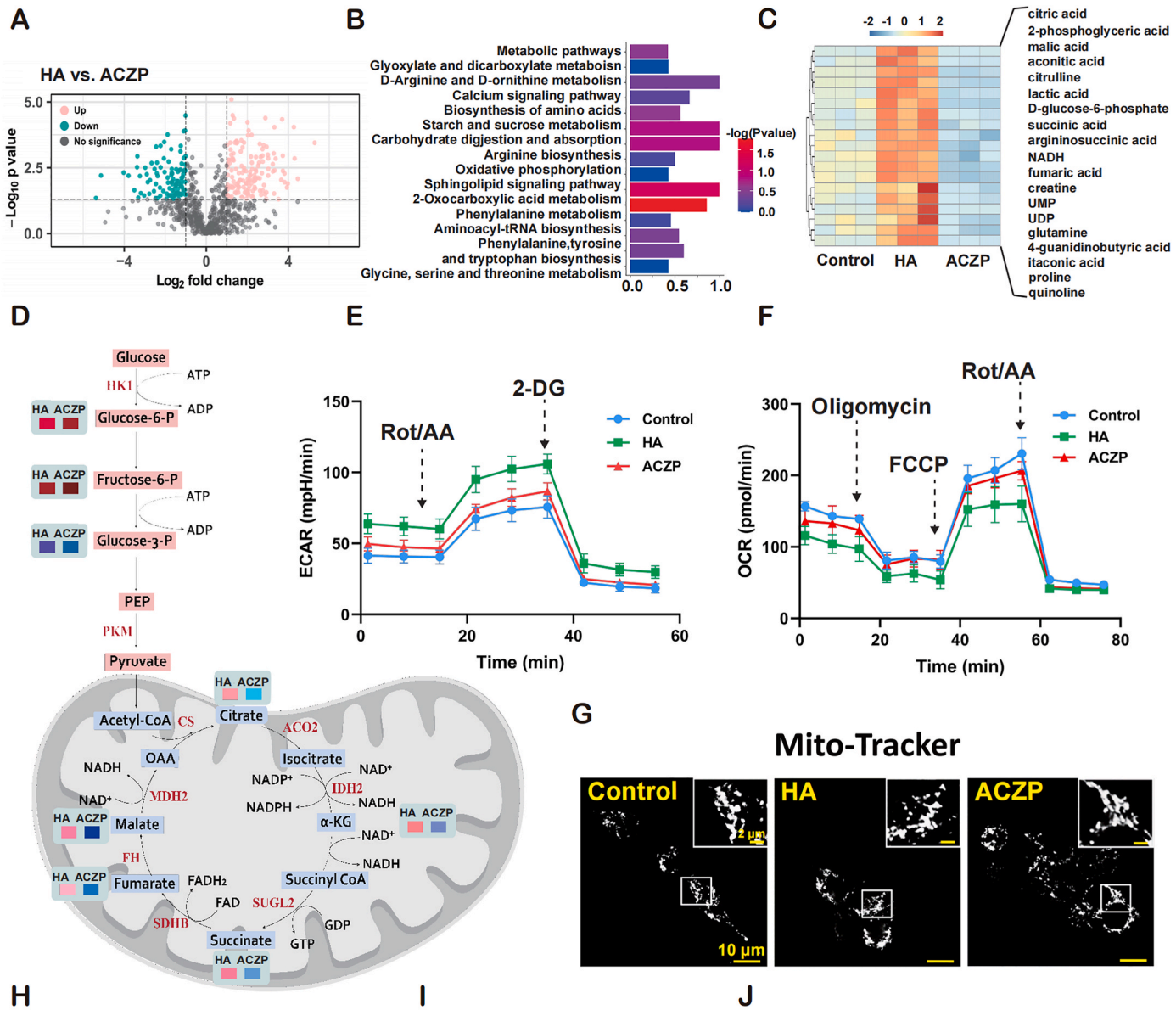

(caption on next page)

Fig. 4. Combining metabolomics and metabolic analysis to explore the ability of ACZP to regulate macrophage energy metabolism and mitochondrial homeostasis: (A) Volcano plot showed the differential metabolites in the macrophages between the HA and ACZP groups. The x axis represented the fold change, and the y axis represented a log-transformed *P*-value. (B) KEGG Pathway enrichment analysis of differential signaling pathway. (C) Heatmap showed the differential metabolites among the Control, HA and ACZP groups. (D) A schematic diagram showed the changes in key metabolites involved in glycolysis and the TCA cycle. (E) ECAR analyzed by macrophages with or without stimulation with HA or ACZP. (F) OCR analyzed by macrophages with or without stimulation with HA or ACZP. (G) Morphological changes in the mitochondrial network shown by the Mito-Tracker specific staining (scale bar: 10 μm; 2 μm (inset)). (H) Changes in macrophage MMP and morphological analysis after JC-1 staining following the addition of nanomaterials. Green fluorescence represents the aggregation of JC-1, while red fluorescence represents the JC-1 monomers in the cytoplasm. (scale bar: 20 μm). (I) Representative images of the co-localization of mitochondria and lysosomes in macrophages stained with the Mito-Tracker (green) and Lyso-Trackero (red). (scale bar: 20 μm). (J) Representative immunofluorescence image of NLRP3 staining (green) in macrophages treated with different nanomaterials. (scale bar: 20 μm (up); 10 μm (down)).

of mitochondrial calcium in the ACZP group was lower than that in the HA group, when macrophages were labeled with the Rhod-2 probe, suggesting that ACZP may play a regulatory role in mitochondrial calcium homeostasis (Fig. S12E). Changes in IP3R protein expression within the ER may be closely linked to Zn^{2+} ameliorating the pro-inflammatory environment of macrophages induced by Ca^{2+}.

Immuno-electron microscopy further corroborated these findings (Fig. 5F). In the HA group, there was an increase in the expression of the mitochondrial membrane protein MCU and the ER protein IP3R, accompanied by mitochondrial swelling and disintegration. Conversely, the antigen was scarcely detectable in the cytoplasm in cells treated with ACZP, and the mitochondria maintained a normal morphology. Additionally, TEM revealed that the contact area between the swollen mitochondria and the ER was increased in the HA group, along with significant alterations in mitochondrial perimeter and morphology (Fig. 5H–J). These results suggest that Zn^{2+} enhance the inflammatory microenvironment via the IP3R/MCU mitochondrial axis and regulate calcium homeostasis (Fig. 5K).

2.6. *In vivo* bone regeneration by the immunomodulatory-driven ACZP for alveolar bone defect repair

To investigate the bone regeneration-promoting effects of ACZP *in vivo*, we established a rabbit mandibular alveolar bone defect model. This model was created by extracting the mandibular first premolars and implanting HA and ACZP for comparison. Bone defects without material implantation served as the Control group (Fig. 6A). Micro-CT imaging was conducted to compare the different samples during the repair of rabbit alveolar bone defects. The bone parameters (BV/TV) of the micro-CT of each group at 4 and 12 weeks were quantitatively analyzed to evaluate the bone mass. The trabecular bone parameters were quantitatively investigated to evaluate the bone microstructure and osteocyte activity characteristics. Four weeks post-surgery, micro-CT images indicated that the bone defects in the ACZP group were filled with 49.01 ± 2.11 % of bone tissue, which increased to 65.96 ± 6.31 % at 12 weeks. In contrast, the HA group exhibited less bone formation, with BV/TV ratios of 46.00 ± 5.69 % after 12 weeks. The Control group showed minimal new bone formation, with a BV/TV of 30.40 ± 1.60 %. Additionally, the average trabecular number (Tb.N) of the newly formed alveolar bone in the ACZP group at 4 and 12 weeks (1.53 ± 0.11 mm^{-1}, $P < 0.01$; 2.99 ± 0.64 mm^{-1}, $P < 0.01$) was greater than in the other groups. Trabeculae thickness (Tb.Th) was the highest in the ACZP group at 4 and 12 weeks, consistent with the results for Tb.N, indicating ACZP promoted the formation of trabecular bone at the alveolar bone defect site. Trabecular separation (Tb.Sp) was the average width of the medullary cavity between trabeculae, which increased during bone resorption. Tb.Sp was also the lowest in the ACZP group (0.12 ± 0.06 μm at 12 weeks), which was nearly half that of the Control group (0.24 ± 0.04 μm, $P < 0.01$) (Fig. 6B–E).

H&E and Masson staining further confirmed the micro-CT results (Fig. 6B and C). At week 4, the amount of endosteal bone growth in the Control group was minimal. In the defect area of the ACZP group, newly formed vascularized bone was observed. In the HA group, there was relatively severe inflammation at the center of the defect. Conversely, in the Control group, only a small amount of new bone formation was observed at the edge of the defect, and there was little new bone in the center. The bone growth in each group at week 12 was greater than that at week 4. In the ACZP group, the defect was almost filled with new bone tissue, and the pattern of collagen fibers was similar to that of natural bone. These results indicate that ACZP implantation can effectively promote the repair of complex alveolar bone defects. Histological examination using H&E staining revealed no significant inflammation or damage in the heart, liver, spleen, lungs, or kidneys. These findings indicate that ACZP nanoparticles possess excellent biosafety *in vivo* (Fig. S13A).

After 4 weeks, triple immunofluorescence staining of CD68, IP3R, and MCU was performed to observe the changes in macrophages in the bone defect area. Fluorescence images and the results from quantitative analysis were demonstrated, the expression levels of IP3R and MCU in macrophages increased significantly in the HA group, which decreased significantly in the ACZP group (Fig. 6F–S13B). These results indicated that Zn^{2+} significantly inhibited the expression o f MCU/IP3R in macrophages in the defect area, supporting the repair and regeneration of the bone defect.

3. Discussion

Timely repair of alveolar bone defects is crucial for restoring normal dental function and optimizing life quality for patients [26]. The composition and structure of repair materials, particularly their similarity to natural bone tissue, are key factors influencing their biological functionality and overall repair efficacy [27,28]. Currently, HA has been widely used as a bioactive bone substitute material in contemporary orthopedics, trauma, and maxillofacial surgery [29,30]. Clarifying the changes in immune cell behavior induced by HA is crucially important for the development of alveolar bone repair materials [31–33]. Our research findings indicate that after HA implantation, the number of pro-inflammatory macrophages in the defect area significantly increases. Lin et al. performed scRNA-seq on mouse mandibular alveolar bone and revealed that macrophages were the largest cell population that interacts with MSCs [13]. Compared to long bone marrow, the proportion of activated macrophages in alveolar bone marrow was higher, suggesting the critical role of macrophages in alveolar bone defects. ACP, an intermediate phase in the formation of HA, plays a critical role in tissue mineralization and has shown significant potential in bone repair, making it an ideal material for tissue regeneration [34]. ACP is degradable and more susceptible to macrophage phagocytosis, thus enhancing its efficacy in bone repair depends on stabilizing the amorphous state and improving anti-inflammatory regulation [35].

Regulating macrophage phenotypes may be more critical than merely managing the overall number of macrophages in bone defects [36]. Macrophages expend substantial energy during phagocytosis and secretion, and their polarization is significantly influenced by metabolic processes [37]. Research has shown that glycolysis activation is linked to pro-inflammatory polarization, while OXPHOS is associated with anti-inflammatory polarization [38]. Our study, using multi-omics techniques like scRNA-seq, metabolomics assays, and OCR/ECAR measurements, revealed that HA implantation primarily activates the glycolytic pathway in macrophages, inhibiting OXPHOS and promoting the pro-inflammatory phenotype. This leads to lactate accumulation,

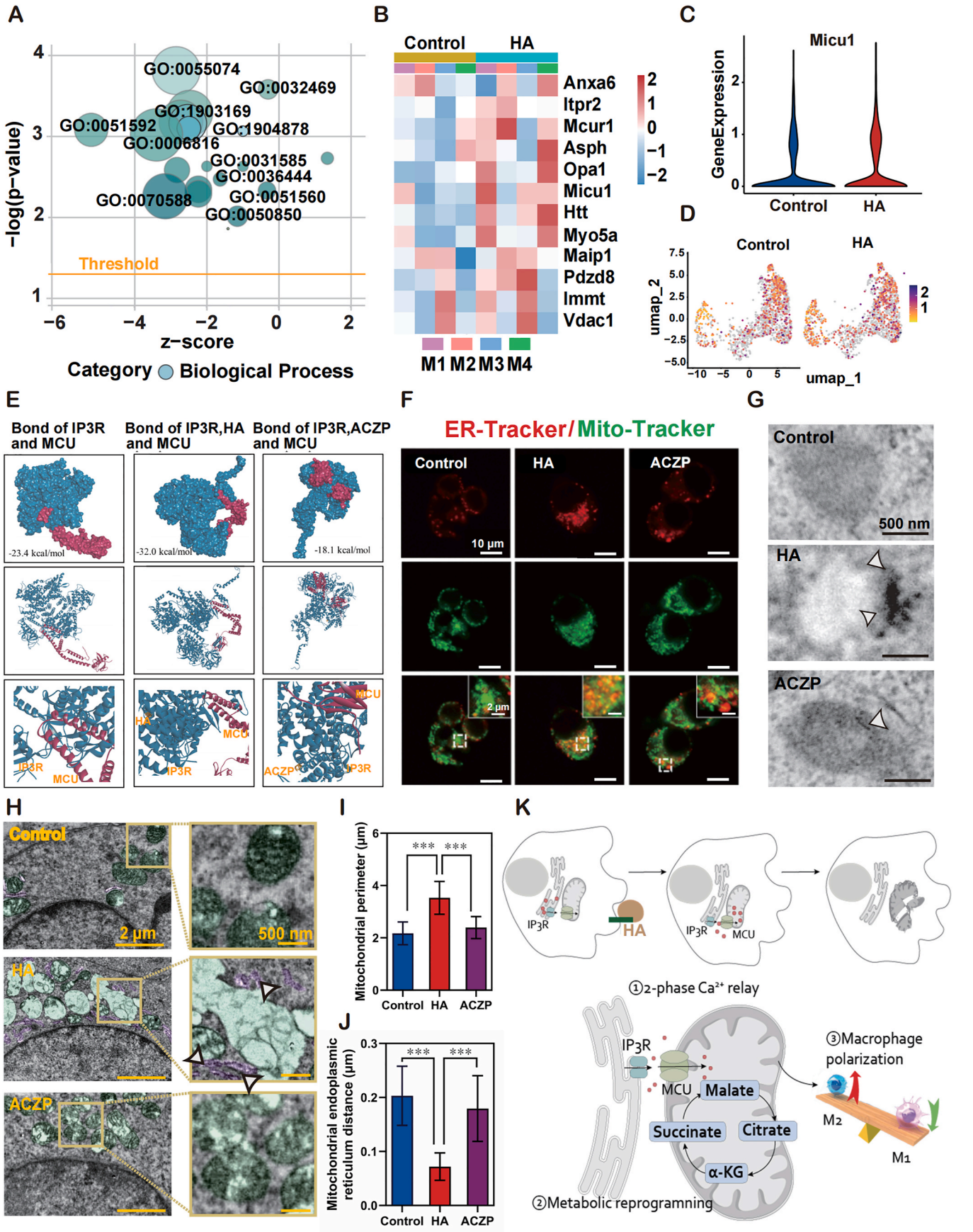

(caption on next page)

Fig. 5. ACZP reverses the pro-inflammatory polarization phenotype of macrophages induced by HA through inhibiting the IP3R/MCU axis: (A) GO bubble plots showed the calcium ion transport-related biological function differences of macrophages between the HA and Control groups. Dot size and color correspond to the enrichment *P*-value of that term (after -log10 transformation). (B) Heatmap of the expression of calcium ion transport-related genes in all macrophage clusters between the HA and Control groups. (C) Violin plot of the expression of the *Micu1* gene in macrophages of the HA and Control groups. (D) UMAP atlas showed the expression of *Micu1* in macrophages of the HA and Control groups. (E) Two-dimensional image of IP3R and MCU molecular with or without HA or ACZP docking simulation. (F) Representative images of the co-localization of the mitochondria and ER in macrophages stained with the Mito-Tracker and ER-Tracker (green: mitochondria; red: ER; scale bar: 10 μm; 2 μm (inset); The arrow pointed to the MAMs structure.). (G) Immuno-electron microscopy showed the expression of IP3R and MCU antibodies between the mitochondria and ER. (scale bar: 500 nm). (H) The morphology of the mitochondria and ER of Control, HA and ACZP groups were analyzed by TEM, and the representative images were displayed. (green: mitochondria; purple: ER; scale bar: 2 μm (left); 500 nm (right)). (I–J) The distance between the ER and mitochondria (n = 30) and the mitochondrial perimeter (n = 30) were quantified and analyzed, respectively. The data were shown as the mean ± SD; $^{*}P < 0.05$; $^{**}P < 0.01$; $^{***}P < 0.001$ indicated significant differences between the indicated columns (one-way ANOVA). (K) Schematic diagram of the calcium ion transport channel between the mitochondria and ER in macrophages.

which further exacerbates mitochondrial dysfunction. The accumulation of lactate products is particularly important in the pro-inflammatory function of HA. pro-inflammatory macrophages produce a large amount of glucose through aerobic glycolysis, inhibiting mitochondrial respiration and leading to adaptive electron transfer. Pyruvate lactate dehydrogenase (LDH) and lactate production stabilize HIF-1α, ultimately exacerbating damage to the respiratory chain [39]. These results suggest that HA may induce rapid metabolic reprogramming by disrupting the OXPHOS function of macrophages.

Mitochondria, essential organelles involved in calcium signaling, energy metabolism, and oxidative stress regulation, play a crucial role in controlling macrophage phenotypes [40]. Our findings indicated that HA implantation disrupted macrophage mitochondrial homeostasis, leading to enhanced mitochondrial membrane potential, abnormal mitophagy, and excessive mtROS accumulation, factors contributing to pro-inflammatory polarization. Mitochondrial dysfunction promotes mtROS generation, stabilizing HIF1-α and promoting the pro-inflammatory phenotype. Zinc ions, known for their ability to scavenge mtROS, can mitigate this effect, enhancing mitochondrial function and promoting macrophage homeostasis [41]. Additionally, HA promoted NLRP3 inflammasome activation in macrophages, leading to inflammatory cytokine release. The NLRP3 inflammasome serves as a platform for the activation of Caspase-1 and the release of IL-1β. Pro-inflammatory signaling pathways initiated by various signals converge on the activation of the NLRP3 inflammasome complex, and mitochondria are the key mediators of NLRP3 activation [42]. ACZP reversed these changes, alleviated inflammation, maintained mitochondrial integrity, and promoted anti-inflammatory polarization. Evidently, HA triggers a series of negative effects in the immune microenvironment, exacerbating mitochondrial dysfunction and interfering with macrophage polarization, while zinc acts as a “brake”, restoring macrophage mitochondrial function and promoting efficient repair [43]. Recent studies have emphasized the role of zinc in osteogenesis, which can stimulate the proliferation and differentiation of osteoblasts, inhibit osteoclast activity, and is involved in immune regulation and enzyme activation [43,44]. Furthermore, zinc supports bone repair by regulating the apoptosis and function of macrophages [45]. Xu et al. developed a nanomedicine, zinc-doped ascorbic acid-derived carbon dots, which simultaneously restored mitochondrial function and subsequently reprogrammed macrophages from the pro-inflammatory to the anti-inflammatory phenotype [46].

MAMs are intricate structures characterized by physical connections between organelles. The interaction between the ER and mitochondria significantly regulates the metabolism of macrophages [47,48]. The function of mitochondria is not isolated; instead, dynamically adapts to various environmental changes through interactions with the ER [49]. IP3R serves as a channel for the release of calcium ions from the ER, typically binding to IP3 to facilitate the entry of calcium ions into the cytoplasm. When interconnected with voltage-dependent anion channel (VDAC) via glucose-regulated protein 75 (GRP75), IP3R can release calcium ions directly from the ER without the need for IP3 binding. An increase in calcium concentration within the intermembrane space activates the MCU located in the inner mitochondrial membrane, promoting efficient calcium uptake by mitochondria, which may lead to calcium overload [50]. Baik et al. reported that various classical activators of NLRP3 are capable of displacing HK2 from VDAC on the outer mitochondrial membrane in macrophages. This upstream signaling event triggers a cascade involving calcium influx into the mitochondria and the assembly of VDAC monomers into oligomeric pores, which serve as a platform for the fully activated NLRP3 inflammasome [51]. Our scRNA-seq analysis indicates that the expression of the pro-inflammatory state in macrophages and the emergence of mitochondrial dysfunction is associated with HA-enhanced IP3R/MCU complexes. However, ACZP has been found to restore calcium homeostasis by reducing the interaction between IP3R and MCU, thereby promoting anti-inflammatory polarization. *In vivo* experiments confirmed that ACZP enhanced alveolar bone defect repair in New Zealand white rabbits, which suggested that ACZP, as a novel bone tissue engineering material, hold significant promise for repairing alveolar bone defects. No biological toxicity was observed *in vivo* for either nanoparticles. Although new bone formation occurred in all groups of rabbits implanted, which was most pronounced in the group of rabbits implanted with ACZP. H&E and Masson staining also demonstrated the excellent bone-promoting ability of ACZP. In addition, the ACZP group exhibited a significantly lower expression of MCU and IP3R in macrophages than the HA group *in vivo*. Therefore, this study elucidated the complex mechanisms underlying the effects of HA on alveolar bone repair and demonstrated the potential of ACZP to enhance tissue repair, offering a foundation for advanced bone tissue engineering.

4. Conclusion

We employed scRNA-seq to investigate the effects of HA on cellular behavior during alveolar bone repair, with a particular focus on macrophage heterogeneity, physiological function, and cell-cell communication. During the bone remodeling process, HA disrupted the mitochondrial metabolic switch of macrophages from glycolysis to OXPHOS, thereby inhibiting the repolarization of macrophages from the pro-inflammatory phenotype to the anti-inflammatory phenotype and affecting the osteogenic effect. The synthesized ACZP protected mitochondrial function by regulating the IP3R/MCU pathway, restored mitochondrial metabolism and homeostasis, and promoted the anti-inflammatory polarization of macrophages, ultimately facilitating the restoration of physiological bone remodeling. These findings underscore the critical role of metabolically active ions in cell-material interactions and highlight the importance of understanding mitochondrial behavior and homeostasis for the design of biomaterials that promote alveolar bone healing.

5. Materials and methods

5.1. Single-cell RNA sequencing

We performed scRNA-Seq analysis on the alveolar bone of mice (Changsheng Laboratories, LN, CN, weighing 300–350 g) 7 days after tooth extraction with or without material implantation (approved by

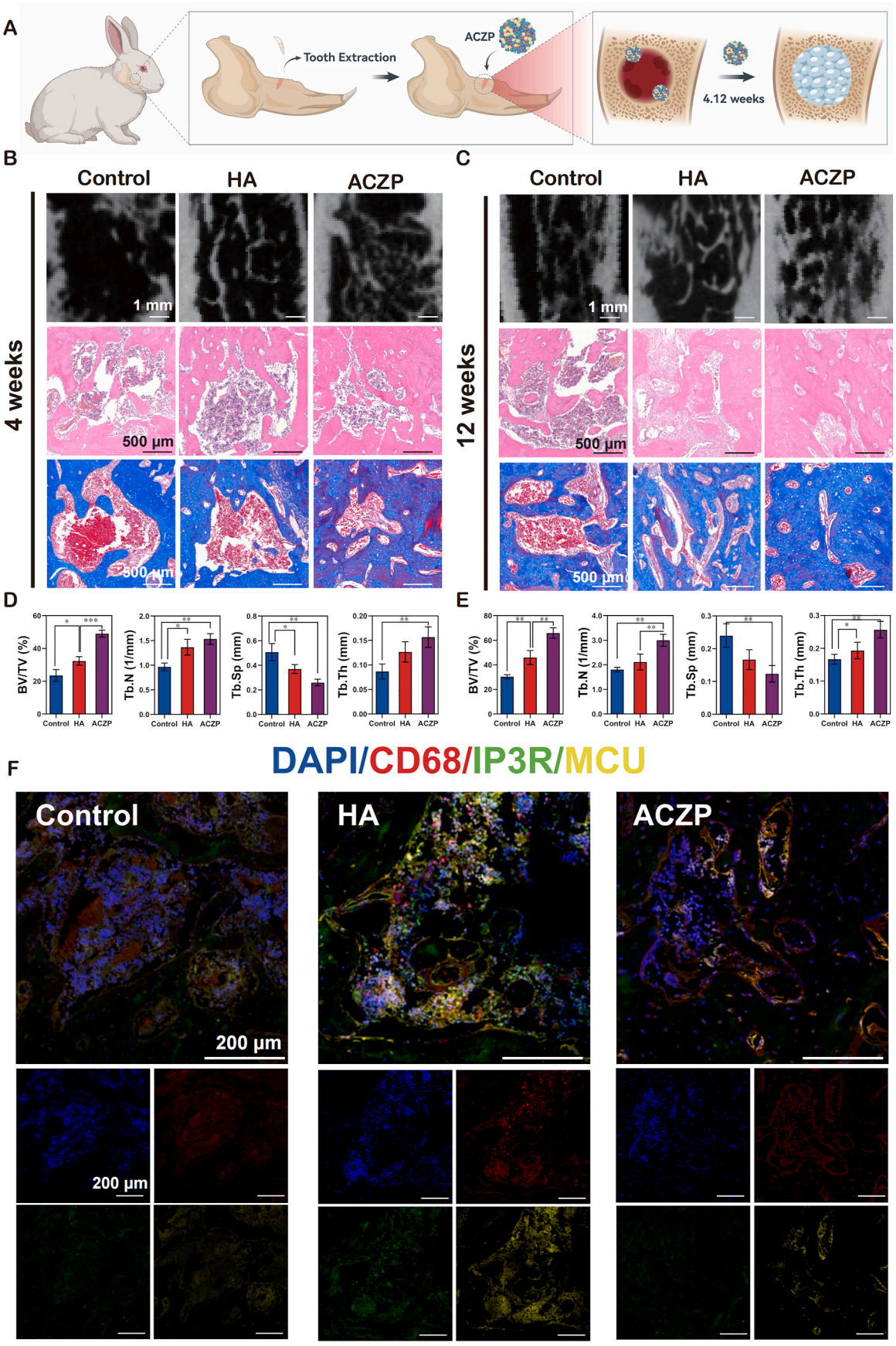

(caption on next page)

Fig. 6. ACZP promotes the repair of alveolar bone defects in New Zealand white rabbits: (A) Schematic diagram of nanomaterials for treating rabbit alveolar bone defects. (B) Representative Micro-CT, H&E, and Masson staining of rabbit alveolar bone 4 weeks after implantation in the Control group, HA group and ACZP group (scale bar: 1 mm (Micro-CT); 500 μm (H&E and Masson staining)). (C) Representative Micro-CT, H&E, and Masson staining of rabbit alveolar bone 12 weeks after implantation in the Control group, HA group and ACZP group (scale bar: 1 mm (Micro-CT); 500 μm (H&E and Masson staining)). (D–E) Semi-quantification of BV/TV, Tb.N, Tb.Th and Tb.Sp in different groups at 4 (left) and 12 (right) weeks. ($n = 3$). The data were shown as the mean ± SD ($n = 3$); *$P < 0.05$; **$P < 0.01$; ***$P <$ 0.001 indicated significant differences between the indicated columns (one-way ANOVA). (F) Representative immunofluorescence image of MCU staining (yellow) and IP3R staining (green) in alveolar bone defect after 4 weeks of implantation. (scale bar: 200 μm).

China Medical University (approval number: KT20250700)). Following the administration of anesthesia, an incision was performed in the area surrounding the maxillary first molar. The molar was carefully extracted utilizing a syringe needle, after which HA was either applied or omitted. Seven days after the surgical procedure, the alveolar bone within the operated site was minced into pieces smaller than 1 mm^3 and subsequently digested in Alpha-modified eagle medium (α-MEM; Gibco, MA, USA) enriched with collagenase II (1 mg/mL), dispase (1 mg/mL), and deoxyribonuclease I (DNase I; Gibco, MA, USA) at a concentration of 10 U/mL. The resultant filtered cells underwent treatment with red blood cell lysate for 1 min and were then washed twice with phosphate-buffered saline (PBS; Thermo Fisher, MA, USA). The cell suspension was permitted to sediment for 2 min. The concentration of cells was modified to 1000 cells/μL using PBS. Approximately 20,000 cells were introduced into the instrument to capture around 10,000 target cells per the instructions provided by the manufacturer. The cDNA library was subsequently stored at −80 °C.

5.2. Sequencing data analysis

The FastQ output files generated from the 10x Chromium sequencing were meticulously aligned using the Cell Ranger software (10x genomics, CA, USA). The quality control process involved filtering out cells characterized by a mitochondrial DNA content exceeding 5 %, those with an expression of more than 7500 genes, and cells that expressed fewer than 200 genes. Following these stringent filtering criteria, the resulting expression matrix was imported into the Seurat software (Satija Lab, NY, USA) package for further analysis. In this context, genes that were expressed in more than three cells were considered validly expressed. Comprehensive data analysis was then executed using the Seurat alignment method in conjunction with canonical correlation analysis (CCA) to ensure accurate interpretation of the results. The identification of highly variable genes (HVGs) was carried out using the FindVariableGenes function within the Seurat package. Using these identified HVGs, dimensionality reduction techniques, specifically UMAP or t-SNE, were employed for effective data visualization. To pinpoint marker genes associated with each specific cluster, the FindAllMarkers function within Seurat was utilized. This analysis was restricted to genes that achieved an adjusted *P*-value of less than 0.05, as determined by the Wilcoxon rank-sum test, ensuring the statistical significance of the identified markers. Following the identification of these marker genes, GO enrichment analyses were conducted leveraging the capabilities of the ClusterProfiler package. Only those GO terms that presented a corrected *P*-value of less than 0.05 were deemed significantly enriched, highlighting the biological relevance of the marker genes in the context of the study.

In addition, the analysis of cell-cell communication was carried out using CellPhoneDB2, a specialized Python-based tool designed for calculating interactions between ligands and receptors across various cell populations. Initially, the mouse MGI symbols were converted to human HGNC symbols utilizing the BioMart package, which facilitated the subsequent application of CellPhoneDB2 for comprehensive analysis of intercellular interactions. Moreover, a detailed single-cell trajectory analysis was performed using the Monocle2. Before initiating the monocle analysis, we rigorously selected marker genes based on the outcomes of Seurat clustering and utilized raw expression counts from the filtered cells. Following the pseudotime analysis, we implemented branch expression analysis modeling (BEAM) to investigate the expression patterns of genes linked to branch fate determination, thereby enriching our understanding of the developmental trajectories within the studied cell populations.

5.3. Preparation of HAP, 5Zn-ACP, 10Zn-ACP, and 20Zn-ACP nanoparticles

The preparation of nano-hydroxyapatite materials refers to previous research work [23]. 5Zn-ACP, 10Zn-ACP, and 20Zn-ACP nanoparticles were prepared using the wet chemical precipitation method. $CaCl_2{\cdot}2H_2O$ (concentration: 0.095 mol/L, 0.090 mol/L, 0.080 mol/L) and $ZnCl_2$ (concentration: 0.005 mol/L, 0.010 mol/L, 0.020 mol/L) were dissolved in 50 mL of ultrapure water to obtain Solution A. The powder of $(NH_4)_2HPO_4$ (concentration: 0.167 mol/L) and PAA (concentration: 1.5 mmol/L) was dissolved in 200 mL of ultrapure water with the molar ratio of 1.5 (the total amount of calcium and zinc to phosphorus). The pH of the solution was adjusted to 9 with ammonium hydroxide solution to obtain Solution B. Solution A was slowly added dropwise to Solution B (rate 2 mL/min) and stirred at 300 rpm for an hour. After 1 h of reaction, the resultant precipitates were collected by centrifugation (5000 rpm, 5 min) and subjected to dialysis (MWCO: 8000–14000 Da) against deionized water for 24 h to eliminate residual reactants and PAA. The purified products were ultimately obtained through freeze-drying for 12 h.

5.4. Characterization of the nanoparticles

The morphology of the samples was observed using TEM (FEI, OR, USA) at an accelerating voltage of 200 kV. The electron diffraction patterns of the particles were recorded with a selected-area aperture, featuring a circular area of 100 nm in diameter. The crystalline structure of the samples was identified through powder XRD, conducted at 40 kV and 100 mA over a 2θ range of 20°–70°, with a step size of 0.02°, utilizing a Rigaku D/max 2400 diffractometer (D-max 2400 diffractometer, Rigaku, TYO, JP) equipped with monochromatic Cu Kα radiation (Kα1 = 1.5418 Å). Infrared transmission spectra of the powders were obtained using a Fourier transform infrared spectrometer (Tensor 27, MA, USA) to identify the functional groups present in the samples, with a wavenumber range from 4000 to 400 cm^{-1} and a step size of 4 cm^{-1}. The contents of calcium and zinc in the nanoparticles were analyzed using XPS (ESCALAB 250, Thermo Fisher, MA, USA). All XPS peaks were calibrated to the standard carbon C1s binding energy (284.6 eV). The data were compared with the NIST X-ray Photoelectron Spectroscopy Database and analyzed using XPSPEAK 4.1 software. The background of the XPS spectra was subtracted using the non-linear, iterative Shirley method. The TGA/DSC of the ACZP samples were analyzed using a thermal analyzer with 10 °C/min from room temperature to 700 °C in an atmospheric environment (STA 449F3, Netzsch, BY, GER). The particle size and zeta potential of HA powders were analyzed by a dynamic light scattering (DLS) device (Malvern Panalytical, Worcs, UK). 5Zn-ACP nanoparticles were dissolved into PBS solution to simulate release *in vivo*. 5Zn-ACP nanoparticles were dissolved in ultrapure water for 10 min, 1 day, 3 days, 5 days, 7 days, 15 days and 30 days to simulate degradation. The Ca^{2+} and Zn^{2+} ion contents were measured using ICP-MS (Prodigy, Leeman Labs, NJ, USA) for each sample.

5.5. Culture of RAW264.7 cells

The mouse macrophage cells RAW264.7 (Cyagen Biosciences, CA, USA) were maintained at 37 °C in Dulbecco's modified Eagle's medium (DMEM; Gibco, MA, USA) supplemented with 10 % fetal bovine serum (FBS; Gibco, MA, USA) and 1 % penicillin-streptomycin (PS; Gibco, MA, USA) to achieve optimal growth conditions.

5.6. Macrophage proliferation and polarization experiments

Prior to the experiment, the materials were placed in a 24-well cell culture plate and soaked in pre-treated culture medium. When the cells reach 80 % confluence, macrophages are collected using cell scraping method and co-cultured with various materials for a total of 3 days. After the co-culture period, RAW264.7 cells underwent a staining treatment using a live/dead cell assay kit (Thermo Fisher, MA, USA). The cells were then observed and analyzed under a fluorescence microscope (Axio Imager.d2; Zeiss, BW, GER) to evaluate the ratio of live cells (green) to dead cells (red) and to assess cell viability. The number of proliferating cells was quantified using CCK-8 (Dojindo, FP, JP). RAW264.7 cells were co-cultured with various materials for 1, 2, and 3 days. The absorbance was measured at 450 nm using an enzyme-linked immunosorbent assay reader (SynergyNeo2, Biotek, VA, USA) to quantify cell proliferation.

To enhance the understanding of macrophage polarization on various materials, an in-depth phenotypic analysis was conducted using immunofluorescence staining. After co-culture for 3 days, RAW264.7 cells were fixed with 4 % paraformaldehyde (PFA; Gibco, MA, USA) at 4 °C for 15 min, followed by membrane permeabilization with 0.1 % Triton X-100 (Thermo Fisher, MA, USA) for 15 min. Subsequently, the cells were incubated with a blocking solution containing 1 % bovine serum albumin (BSA; Gibco, MA, USA) and 0.3 M glycine in PBS for an hour to minimize non-specific binding. Primary antibodies against Arg1 and iNOS (Thermo Fisher, MA, USA; 1:200 dilution) were added to the samples and incubated overnight at 4 °C to label specific markers for anti-inflammatory and pro-inflammatory macrophages, respectively. Following 24 h incubation, samples were sequentially processed with PBS washing and exposure to fluorescein isothiocyanate or tetramethylrhodamine isothiocyanate (Thermo Fisher, MA, USA; 1:200 dilution) at 37 °C for 1 h. Nuclear staining with 4′,6-diamidino-2-phenylindole (DAPI; Thermo Fisher, MA, USA) was performed to trace the cell nuclei. The samples were then observed using confocal microscopy using 350 nm laser (LSM 900, Zeiss, BW, GER).

5.7. Mitochondrial metabolic status

Samples were analyzed by liquid chromatography-mass spectrometry (LC-MS; Luming Biotech, SH, CN) with raw data processing through Progenesis QI software (Waters Corporation, MA, USA) under the following parameters: a precursor tolerance of 5 ppm, fragment tolerance of 10 ppm, and retention time (RT) tolerance of 0.02 min. During peak RT comparison, internal standard detection parameters were disabled, isotopic peaks were excluded from analysis, noise elimination level was set at 10.00, and a minimum intensity of 15 % of the base peak intensity was applied. An excel file was generated with a three-dimensional (3D) dataset containing *m/z*, peak RT, and peak intensity, using RT-m/z pairs as ion identifiers. To refine the dataset, peaks with missing values (ion strength 0) in over 50 % of the samples were removed, with internal standards utilized for data quality control (reproducibility).

5.8. Analysis of cell bioenergetics

The OCR and the ECAR were measured using a Seahorse XFe96 Analyzer (Agilent, CA, USA), following the manufacturer's instructions. Briefly, RAW264.7 cells were seeded in 96-well Seahorse assay plates at a concentration of 1.5×10^5 cells/well, and cultured overnight for attachment. Correction is required for cell densities that vary from well to well at the time of the final assay (e.g., primary cell plating, between two plates, intervention treatments affecting cell growth between different groups). Count with Hochest staining, and calculate the corresponding number of cells per well after dividing by normalized units. For measuring the OCR and the ECAR in RAW264.7 cells co-cultured with various materials, cells were washed once with PBS and cultured in the indicated medium for 4 h before changing to Seahorse medium. Oligomycin (1 μM; Cayman Chemicals, TX, USA), carbonyl cyanide-p-trifluoromethoxyphenylhydrazone (FCCP, 1 μM; Santa Cruz Biotechnology, TX, USA), rotenone/antimycin A (Rot/AA, 500 nM; Sigma–Aldrich, MO, USA), and 2-deoxy-D-glucose (2-DG, 25 mM; Sigma–Aldrich, MO, USA) were formulated in XF assay medium. These compounds were then introduced into the designated injection ports on the cartridge plate and allowed to incubate for 10 min at 37 °C in a non-CO_2 incubator. Presto Blue™ assays (Thermo Fisher, MA, USA) were used to evaluate cell viability and normalize readings from the Seahorse XF Analyzer.

5.9. Measurement of mitochondrial morphology and structure

Cells cultured on 100 mm dishes underwent two washes with PBS and were subsequently fixed in a solution containing 3 % PFA and 0.25 % sucrose in 0.1 M sodium phosphate buffer for 1 h at room temperature. The cells were then scratched, collected, and subjected to gradient centrifugation to concentrate them. The samples underwent postfixation with 2 % uranyl acetate at 4 °C overnight. Dehydration of samples was performed using varying concentrations of ethanol, followed by polymerization at 60 °C over a duration of two days. Using an ultramicrotome (Leica, HE, GER), the blocks were sliced into ultrathin sections measuring 70 nm with a diamond knife. These sections were mounted on copper grids and stained with 2 % lead citrate at room temperature for 15 min, followed by 2 % uranyl acetate at room temperature for 10 min. Lastly, the sections underwent standard procedures for electron microscopy. Images were captured using a TEM (FEI, NH, USA). The mitochondrial morphology and structure were visualized utilizing the TEM and subsequently analyzed with ImageJ software (NIH ImageJ system; National Institutes of Health, MD, USA).

5.10. Mitochondrial function

As per the manufacturer's instructions, the JC-1 MMP assay kit (G-clone, BJ, CN) was utilized to determine the MMP of macrophages. The cells underwent incubation, followed by two washes with PBS, and then incubatedion with JC-1 staining solution at 37 °C for 20 min. After that, the cells were washed twice with JC-1 dilution buffer and immediately observed under a confocal laser microscope (BX51; Olympus Optical, TYO, JP).

For cellular organelle fluorescence staining, the ER-Tracker (Thermo Fisher, MA, USA) and Mito-Tracker (Thermo Fisher, MA, USA) double staining were used to evaluate the morphology of the ER and mitochondria co-localization in RAW264.7 cells. Briefly, RAW264.7 cells were incubated at 37 °C for 30 min in α-MEM containing 1×10^{-3} mol/L ER-Tracker and 100×10^{-9} mol/L Mito-Tracker. The Lyso-Tracker (Yeasen Biotech Co, Ltd, SH, CN) and Mito-Tracker double staining were utilized to the morphology of the lysosomes and mitochondria co-localization in RAW264.7 cells. The cells were incubated at 37 °C for 40 min in α-MEM containing 50×10^{-9} mol/L Lyso-Tracker and 100×10^{-9} mol/L Mito-Tracker added. After washing, replace the culture medium with fresh α-MEM. For live-cell imaging, the samples were then observed using confocal microscopy using 350 nm laser (LSM 900, Zeiss, BW, GER). Cell cultures were maintained at 37 °C, 5 % CO_2 throughout acquisition.

5.11. Molecular docking validation

Utilizing AutoDock 1.5.6 (Scripps, CA, USA), the target proteins that underwent pre-treatment were exported in pdbqt format. The compounds were configured to include rotatable bonds and were subsequently saved in pdbqt format for the final calculations of the docking simulations. A binding energy of less than 0 kcal/mol suggests that spontaneous binding occurs between the compound and the target protein, whereas a binding energy of equal to or below −5.0 kcal/mol indicates a strong binding interaction. The docking results identified nine optimal positions, and the conformation with the lowest binding energy along with the highest frequency of clustering was regarded as the most likely binding mode between the ligands and the proteins. The visualization of the docking outcomes was conducted using LigPlot version 4.5.3 (EMBL-EBI, Cambs, UK).

5.12. In vivo implantation of ACZP

The *in vivo* implantation experiment followed the Guide for the Care and Use of Laboratory Animals issued by the Ministry of Science and Technology of China and was approved by the Ethics Committee at China Medical University (approval number: KT20250700). Ten six-month-old male New Zealand white rabbits (Changsheng Biotechnology, SY, CN; 2–3 kg) were anesthetized via intraperitoneal injection of sodium pentobarbital (3 % w/v, 30 mg kg^{-1}). Bilateral mandibular first premolar extraction created standardized alveolar defects, followed by implantation of: 1) HA; 2) ACZP. After 4 and 12 weeks of implantation, all rabbits were sacrificed by overanesthesia with an overdose of intravenous pentobarbital sodium (400 mg/kg), and the mandibles were then detached and fixed in 4 % PFA. Harvested rabbit alveolar bones were scanned using a micro-CT scanner (Xradia 520 Versa, Zeiss, BW, GER) at 45 kV and 200 mA. A region of interest (ROI) was defined using CT Analyser 1.15.2.2 software (Bruker Corporation, MA, USA). Within the ROI, histomorphometric indices, including BV/TV, Tb.N, Tb.Sp, and Tb.Th, were quantitatively analyzed.

The fixed tissue was gently shaken and decalcified with a 10 % ethylenediaminetetraacetic acid (EDTA; Servicebio, HB, CN) solution for 4 weeks. Conventional paraffin embedding after decalcification was performed, and all specimens were kept in the same position as possible. Sections of 4 μm thickness were cut from them. H&E and Masson staining were performed with the H&E dye solution set and Masson dye solution set (Servicebio, HB, CN) for histological evaluation. Sections were incubated overnight with specific antibodies (CD68, MCU, IP3R; Scanco Medical AG, ZH, CH) at 4 °C. Subsequently, the corresponding secondary antibodies were incubated for 50 min at room temperature in the dark. The nuclei were labeled with DAPI.

5.13. Statistical analysis

GraphPad Prism v9.0 (GraphPad Software; San Diego, CA, USA) was used for statistical analyses. Data from at least three independent experiments are presented as means ± SEM. Intergroup comparisons utilized an unpaired two-tailed Student's t-test, whereas multigroup analyses using a one-way analysis of variance followed by Tukey's post hoc tests for multiple comparisons. The significance of the study was defined as a P-value <0.05.

CRediT authorship contribution statement

Shuze Wang: Data curation. **Lei Cao:** Project administration, Investigation. **Caihao Huang:** Methodology. **Junyi Wang:** Writing – original draft. **Jialin Liu:** Validation, Software. **Yeyuan Wang:** Formal analysis. **Qiang Wang:** Writing – review & editing. **Qing Zhou:** Visualization, Funding acquisition. **Xing Zhang:** Supervision, Resources. **Dan Zhang:** Conceptualization.

Ethics approval and consent to participate

The *in vivo* implantation experiment followed the Guide for the Care and Use of Laboratory Animals issued by the Ministry of Science and Technology of China and was approved by the Ethics Committee at China Medical University (approval number: KT20250700).

Declaration of competing interest

The authors declare that they have no known competing financial interests or personal relationships that could have appeared to influence the work reported in this paper.

Acknowledgments

This work was supported partly by the National Key R&D Program of China (No. 2024YFC2418600), the Natural Science Foundation of China (No. 82370987) and the Natural Science Foundation of Liaoning Province (No. 2024-MSBA-66).

Appendix A. Supplementary data

Supplementary data to this article can be found online at https://doi.org/10.1016/j.bioactmat.2025.06.053.

Abbreviation

HA: Hydroxyapatite; **ACZP:** Amorphous calcium zinc phosphate; **OXPHOS:** Oxidative phosphorylation; **GLUT1:** Glucose transporter-1; **HK2:** Hexokinase 2; **PKM2:** Pyruvate kinase M2; **ScRNA-seq:** Single-cell RNA sequencing; **ACP:** Amorphous calcium phosphate; **MSCs:** Mesenchymal stem cells; **IP3:** Inositol trisphosphate; **T_NK cells:** Natural killer T cells; **DCs:** Dendritic cells; **Mono_Mac:** Monocyte_macrophages; **GMP:** Granulocyte-monocyte progenitor; **cDNA:** Complementary DNA; **t-SNE: t-distributed stochastic neighbor embedding; UMAP: Uniform manifold approximation and projection; GO:** Gene Ontology; **mtROS:** Mitochondrial reactive oxygen species; **PAA:** Polyacrylic acid; **TEM:** Transmission electron microscope; **XPS:** X-ray photoelectron spectroscopy; **XRD:** X-Ray diffraction; **β-TCP:** β-tricalcium phosphate; **CCK-8:** Cell counting kit-8; **ALP:** Alkaline phosphatase; **KEGG:** Kyoto Encyclopedia of Genes and Genomes; **OCR:** Oxygen consumption rate; **ECAR:** Extracellular acidification rate; **MMP:** Mitochondrial membrane potential; **NLRP3:** NOD-like receptor thermal protein domain associated protein 3; **ER:** Endoplasmic reticulum; **IP3R:** Inositol 1,4,5-triphosphate receptor; **MCU:** Mitochondrial calcium uniporter; **MAMs:** Mitochondrial-associated membranes; **CO-IP:** Co-immunoprecipitation; **Tb.N:** Trabecular number; **Tb.Th:** Trabeculae thickness; **Tb.Sp:** Trabecular separation; **LDH:** Pyruvate lactate dehydrogenase; **VDAC:** Voltage-dependent anion channels; **GRP75:** Glucose-regulated protein 75; **α-MEM:** Alpha-modified eagle medium; **PBS:** Phosphate-buffered saline; **CCA:** Canonical correlation analysis; **HVGs:** Highly variable genes; **BEAM:** Branch expression analysis modeling; **TGA/DSC:** Thermogravimetric analysis/Differential scanning calorimetry; **DLS:** Dynamic light scattering; **ICP-MS:** Inductively coupled plasma mass spectrometry; **DMEM:** Dulbecco's modified Eagle's medium; **FBS:** Fetal bovine serum; **PS:** Penicillin-streptomycin; **PFA:** Paraformaldehyde; **BSA:** Bovine serum albumin; **DAPI:** 4′,6-diamidino-2-phenylindole; **FCCP:** Carbonyl cyanide-p-trifluoromethoxypheny lhydrazone; **Rot/AA:** Rotenone/antimycin A; **2-DG:** 2-deoxy-D-glucose; **BP:** Biological process; **CC:** Cellular component; **MF:** Molecular function; **LC-MS:** Liquid chromatography-mass spectrometry; **RT:** Retention time; **3D:** Three-dimensional; **ROI:** Region of interest; **EDTA:** Ethylenediaminetetraacetic acid.

References

[1] S. Wei, J. Ma, L. Xu, et al., Biodegradable materials for bone defect repair, Military Medical Research 7 (1) (2020) 54–78.
[2] B. Tan, Q. Tang, Y. Zhong, et al., Biomaterial-based strategies for maxillofacial tumour therapy and bone defect regeneration, Int. J. Oral Sci. 13 (1) (2021) 9–24.
[3] T. Lazarov, S. Juarez-Carreño, N. Cox, et al., Physiology and diseases of tissue-resident macrophages, Nature 618 (7966) (2023) 698–707.
[4] P. Rodríguez-Morales, R.A. Franklin, Macrophage phenotypes and functions: resolving inflammation and restoring homeostasis, Trends Immunol. 44 (12) (2023) 986–998.
[5] E.L. Mills, L.A. O'Neill, Reprogramming mitochondrial metabolism in macrophages as an anti-inflammatory signal, Eur. J. Immunol. 46 (1) (2016) 13–21.
[6] X. Long, M. Liu, Y. Nan, et al., Revitalizing ancient mitochondria with nano-strategies: mitochondria-remedying nanodrugs concentrate on disease control, Adv. Mater. 36 (18) (2024) e2308239.
[7] C.A. Ferreira, D. Ni, Z.T. Rosenkrans, et al., Scavenging of reactive oxygen and nitrogen species with nanomaterials, Nano Res. 11 (10) (2018) 4955–4984.
[8] I. Ielo, G. Calabrese, G. De Luca, et al., Recent advances in hydroxyapatite-based biocomposites for bone tissue regeneration in orthopedics, Int. J. Mol. Sci. 23 (17) (2022) 9721–9745.
[9] P. Proussaefs, J. Lozada, G. Valencia, et al., Histologic evaluation of a hydroxyapatite onlay bone graft retrieved after 9 years: a clinical report, J. Prosthet. Dent 87 (5) (2002) 481–484.
[10] S.V. Dorozhkin, Bioceramics of calcium orthophosphates, Biomaterials 31 (7) (2010) 1465–1485.
[11] L.C. Shanley, O.R. Mahon, S.A. O'Rourke, et al., Macrophage metabolic profile is altered by hydroxyapatite particle size, Acta Biomater. 160 (2023) 311–321.
[12] X. Han, Z. Zhou, L. Fei, et al., Construction of a human cell landscape at single-cell level, Nature 581 (7808) (2020) 303–309.
[13] W. Lin, Q. Li, D. Zhang, et al., Mapping the immune microenvironment for mandibular alveolar bone homeostasis at single-cell resolution, Bone Research 9 (1) (2021) 17–28.
[14] B. Jin, Z. Liu, C. Shao, et al., Phase transformation mechanism of amorphous calcium phosphate to hydroxyapatite investigated by liquid-cell transmission electron microscopy, Cryst. Growth Des. 21 (9) (2021) 5126–5134.
[15] D. Tadic, F. Peters, M. Epple, Continuous synthesis of amorphous carbonated apatites, Biomaterials 23 (12) (2002) 2553–2559.
[16] A. Dion, B. Berno, G. Hall, et al., The effect of processing on the structural characteristics of vancomycin-loaded amorphous calcium phosphate matrices, Biomaterials 26 (21) (2005) 4486–4494.
[17] S. Wang, C. Huang, X. Zhang, et al., Zinc doped amorphous calcium phosphate integrated GBR module role in facilitating bone augmentation via immunostimulation of osteogenesis, J. Mater. Sci. Technol. 226 (2025) 320–333.
[18] A. Raffaello, C. Mammucari, G. Gherardi, et al., Calcium at the center of cell signaling: interplay between endoplasmic reticulum, mitochondria, and lysosomes, Trends Biochem. Sci. 41 (12) (2016) 1035–1049.
[19] A. Lotsari, A.K. Rajasekharan, M. Halvarsson, et al., Transformation of amorphous calcium phosphate to bone-like apatite, Nat. Commun. 9 (1) (2018) 4170–4180.
[20] M. Molenda, J. Kolmas, The role of zinc in bone tissue health and regeneration—a review, Biol. Trace Elem. Res. 201 (12) (2023) 5640–5651.
[21] X. Fu, Y. Li, T. Huang, et al., Runx2/Osterix and zinc uptake synergize to orchestrate osteogenic differentiation and citrate containing bone apatite formation, Adv. Sci. 5 (4) (2018) 1700755.
[22] J. Tan, S. Li, C. Sun, et al., A dose-dependent spatiotemporal response of angiogenesis elicited by Zn biodegradation during the initial stage of bone regeneration, Adv. Healthcare Mater. 13 (4) (2024) e2302305.
[23] M. Hershfinkel, A. Moran, N. Grossman, et al., A zinc-sensing receptor triggers the release of intracellular Ca^{2+} and regulates ion transport, Proc. Natl. Acad. Sci. 98 (20) (2001) 11749–11754.
[24] N. Li, W. Cui, P. Cong, et al., Biomimetic inorganic-organic hybrid nanoparticles from magnesium-substituted amorphous calcium phosphate clusters and polyacrylic acid molecules, Bioact. Mater. 6 (8) (2021) 2303–2314.
[25] L. Cao, I. Ullah, N. Li, et al., Plasma spray of biofunctional (Mg, sr)-substituted hydroxyapatite coatings for titanium alloy implants, J. Mater. Sci. Technol. 35 (5) (2019) 719–726.
[26] A. Shakya, Y. Li, N. Chang, et al., Supra-alveolar bone regeneration: progress, challenges, and future perspectives, Compos. B Eng. 283 (2024) 111673.
[27] M. Wu, H. Liu, Y. Zhu, et al., Bioinspired soft-hard combined system with mild photothermal therapeutic activity promotes diabetic bone defect healing via synergetic effects of immune activation and angiogenesis, Theranostics 14 (10) (2024) 4014–4057.
[28] T.F. Valamvanos, X. Dereka, H. Katifelis, et al., Recent advances in scaffolds for guided bone regeneration, Biomimetics 9 (3) (2024) 153–177.
[29] J. Jobisha, V. Vinisha, B.R. Francy, et al., Multifaceted roles of hydroxyapatite: an extensive overview of synthesis approaches and applications in medicine and industry, Inorg. Chem. Commun. 177 (2025) 114385.
[30] M. Haghshenas, Mechanical characteristics of biodegradable magnesium matrix composites: a review, J. Magnesium Alloys 5 (2) (2017) 189–201.
[31] L. Shang, J. Shao, S. Ge, Immunomodulatory properties: the accelerant of hydroxyapatite-based materials for bone regeneration, Tissue Eng. C Methods 28 (8) (2022) 377–392.
[32] Y. Zhu, H. Liu, P. Wu, et al., Multifunctional injectable hydrogel system as a mild photothermal-assisted therapeutic platform for programmed regulation of inflammation and osteo-microenvironment for enhanced healing of diabetic bone defects in situ, Theranostics 14 (18) (2024) 7140–7198.
[33] M. Wu, H. Liu, Y. Zhu, et al., Mild photothermal-stimulation based on injectable and photocurable hydrogels orchestrates immunomodulation and osteogenesis for high-performance bone regeneration, Small 19 (28) (2023) e2300111.
[34] Y. Yan, Y. Fang, J. Li, et al., Transformation of amorphous calcium phosphate to monoclinic nano-hydroxylapatite, CrystEngComm 24 (40) (2022) 7034–7038.
[35] L. Degli Esposti, M. Iafisco, Amorphous calcium phosphate, the lack of order is an abundance of possibilities, Biomaterials and Biosystems 5 (2022) 100037.
[36] Y. Yuan, X. Han, X. Zhao, et al., Circulating exosome long non-coding RNAs are associated with atrial structural remodeling by increasing systemic inflammation in atrial fibrillation patients, Journal of Translational Internal Medicine 12 (1) (2024) 106–118.
[37] S. Houston, Tissue differences in macrophage metabolism, Nat. Immunol. 24 (3) (2023), 378–378.
[38] P. Li, Z. Fan, Y. Huang, et al., Mitochondrial dynamics at the intersection of macrophage polarization and metabolism, Front. Immunol. 16 (2025) 1520814.
[39] L. Chen, P. Qiao, H. Liu, et al., Amorphous calcium phosphate NPs mediate the macrophage response and modulate BMSC osteogenesis, Inflammation 44 (1) (2021) 278–296.
[40] Z. Tian, X. Wang, S. Chen, et al., Mitochondria-targeted biomaterials-regulating macrophage polarization opens new perspectives for disease treatment, Int. J. Nanomed. 20 (2025) 1509–1528.
[41] Y. Yang, P. Wang, J. Guo, et al., Zinc overload induces damage to H9c2 cardiomyocyte through mitochondrial dysfunction and ROS-mediated mitophagy, Cardiovasc. Toxicol. 23 (11–12) (2023) 388–405.
[42] C. Jin, P. Frayssinet, R. Flavell, NLRP3 inflammasome plays a critical role in the pathogenesis of hydroxyapatite-associated arthropathy, Osteoarthr. Cartil. 20 (2012) S32.
[43] Z. Chen, W. Zhang, M. Wang, et al., Effects of Zinc, Magnesium, and iron ions on bone tissue engineering, ACS Biomater. Sci. Eng. 8 (6) (2022) 2321–2335.
[44] C.A. Shahed, F. Ahmad, E. Günister, et al., Antibacterial mechanism with consequent cytotoxicity of different reinforcements in biodegradable magnesium and zinc alloys: a review, J. Magnesium Alloys 11 (9) (2023) 3038–3058.
[45] K. Kijima, G. Ono, K. Kobayakawa, et al., Zinc deficiency impairs axonal regeneration and functional recovery after spinal cord injury by modulating macrophage polarization via NF-κB pathway, Front. Immunol. 14 (2023) 1290100.
[46] E. Xu, J. Wang, N. Ding, et al., Nanoarchitectonics with Zinc-doped Carbon dots for mitochondria-targeted repair and regeneration signaling amplification in CLI therapy, ACS Appl. Mater. Interfaces 69 (1) (2025) 5c03525.
[47] J.S. Harrington, S.W. Ryter, M. Plataki, et al., Mitochondria in health, disease, and aging, Physiol. Rev. 103 (4) (2023) 2349–2422.
[48] X. Chen, C. Shi, M. He, et al., Endoplasmic reticulum stress: molecular mechanism and therapeutic targets, Signal Transduct. Targeted Ther. 8 (1) (2023) 352–391.
[49] R.A. Magalhães, B.F. Dal, T. Knedlik, et al., Chemical modulation of mitochondria–endoplasmic reticulum contact sites, Cells 9 (7) (2020) 1637–1654.
[50] Y. Chi, Z. Bai, G. Feng, et al., ER-mitochondria contact sites regulate hepatic lipogenesis via Ip3r-Grp75-Vdac complex recruiting Seipin, Cell Commun. Signal. 22 (1) (2024) 464–481.
[51] S.H. Baik, V.K. Ramanujan, C. Becker, et al., Hexokinase dissociation from mitochondria promotes oligomerization of VDAC that facilitates NLRP3 inflammasome assembly and activation, Science Immunology 8 (84) (2023) eade7652.